

Cite this: DOI: 10.1039/xxxxxxxxxx

High-pressure behaviour of Prussian blue analogues: interplay of hydration, Jahn-Teller distortions and vacancies[†]

Hanna L. B. Boström,^a Ines E. Collings,^b Andrew B. Cairns,^c Carl P. Romao,^{a,d} and Andrew L. Goodwin^{*a}

Received Date

Accepted Date

DOI: 10.1039/xxxxxxxxxx

www.rsc.org/journalname

We report a high-pressure crystallographic study of four hydrated Prussian blue analogues: $M[\text{Pt}(\text{CN})_6]$ and $M_3[\text{Co}(\text{CN})_6]_2$ ($M = \text{Mn}^{2+}, \text{Cu}^{2+}$) in the range 0–3 GPa. $\text{Mn}_3[\text{Co}(\text{CN})_6]_2$ was studied by single-crystal X-ray diffraction, whereas the other systems were only available in polycrystalline form. The Mn-containing compounds undergo pressure-induced phase transitions from $Fm\bar{3}m$ to $R\bar{3}$ at ~ 1.0 – 1.5 GPa driven by cooperative tilting of the octahedral units. No phase transition was found for the orbitally disordered $\text{Cu}_3[\text{Co}(\text{CN})_6]_2$ up to 3 GPa. $\text{Mn}_3[\text{Co}(\text{CN})_6]_2$ is significantly softer than the other samples, with a bulk modulus of ~ 14 GPa compared to ~ 35 GPa of the powdered samples. The discrepant pressure responses are discussed in terms of the presence of structural defects, Jahn-Teller distortions, and hydration. The implications for the development of polar systems are reviewed based upon our high-pressure study.

1 Introduction

Prussian blue analogues (PBAs) are an interesting class of cyanide-linked coordination polymers with a diverse range of properties, including spin-crossover behaviour, photoswitchable magnetism, permanent porosity and mass transport abilities of relevance to battery applications.^{1–7} The varied functionality can be attributed to the compositional versatility; PBAs are similar to double perovskites, with the general formula $A_xB_y[B'(\text{CN})_6]_z$, where A (if present) is an alkali metal and B and B' are transition metal ions.⁸ Nearly all first-row—and many second-row—transition metals can be incorporated on the B-sites and the stoichiometry can be varied by changing the oxidation states, rendering PBAs highly tuneable materials.^{9–12} An especially prevalent stoichiometry is $B_3^{2+}[B'^{3+}(\text{CN})_6]_2$, where one third of the $B(\text{CN})_6$ sites are unoccupied and water molecules complete the coordination sphere of the B-site metal.¹³ A less common composition is the defect-free $B^{2+}[B'^{4+}(\text{CN})_6]$,¹⁰ which can be described as a

double ReO_3 topology.

Prussian blue analogues belong to the broad class of molecular perovskites, which—like conventional perovskites—can support octahedral tilting.^{14–16} Tilt modes are classified as rigid unit modes (RUMs), *i.e.* low-energy vibrations that propagate without altering the local geometry of the coordination polyhedra, and which often strongly influence stimuli-induced behaviour.^{17,18} Although molecular perovskites generally tend to exhibit complex series of RUMs, including distortions unfeasible in conventional ceramic perovskites,^{16,19,20} PBAs rarely exhibit condensed RUMs upon cooling. However, octahedral tilting upon compression has been suggested on the basis of spectroscopic evidence.^{21–23} The presence (or absence) of tilts is highly relevant for the functionality of PBAs, as they influence the free pore space, the orbital overlap and the strength of the magnetic correlations.^{23,24} For example, the ferrimagnetic transition temperatures of $A_2\text{Mn}[\text{Mn}(\text{CN})_6]$ increase with pressure, which was speculatively attributed to octahedral tilting, leading to an weakening of the ferromagnetic exchange interactions.²⁴ Another study on cyanide-bridged bimetallic coordination polymers also showed that the ferrimagnetic transition temperature could be increased upon compression and the reduction in M–CN–M linkages was suggested to be the reason for the increase in T_C .²⁵ However, there are relatively few systematic crystallographic high-pressure studies on Prussian blue analogues at present, which would confirm the proposed pressure-induced tilting and enable, for example, magnetostructural correlations to be established.^{22,26,27}

Here, we present a variable-pressure X-ray diffraction study

^a Department of Chemistry, University of Oxford, Inorganic Chemistry Laboratory, South Parks Road, Oxford OX1 3QR, UK. Fax: +44 (0)1865 274690; Tel: +44 (0)1865 272137; E-mail: andrew.goodwin@chem.ox.ac.uk

^b European Synchrotron Radiation Facility, 71 Avenue des Martyrs, 38000 Grenoble, France.

^c Department of Materials, Imperial College London, Royal School of Mines, Exhibition Road, SW7 2AZ, UK.

^d Institut für Anorganische Chemie, Universität Tübingen, Auf der Morgenstelle 18, 72076 Tübingen, Germany.

[†] Electronic Supplementary Information (ESI) available: [details of any supplementary information available should be included here]. See DOI: 10.1039/b000000x/

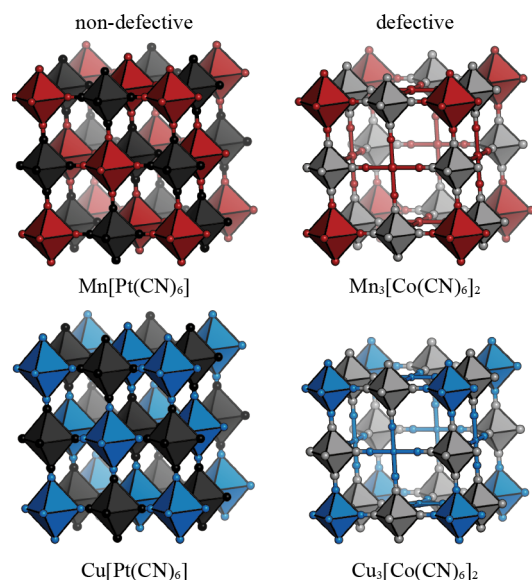


Fig. 1 Representations of the crystal structures of the systems under study. Mn is shown as red polyhedra, Pt as black polyhedra, Co as grey and Cu as blue. The vacancies in $Mn_3[Co(CN)_6]_2$ are shown at the centre of the unit cells. Interstitial water molecules not included for clarity.

of four Prussian blue analogues: namely, $Mn_3[Co(CN)_6]_2$, $Cu_3[Co(CN)_6]_2$, $Mn[Pt(CN)_6]$ and $Cu[Pt(CN)_6]$ [Fig. 1]. The hexacyanocobaltates are defective systems with $Co(CN)_6$ vacancies, whereas the hexacyanoplatinates are considered defect free. Moreover, as $Cu[Pt(CN)_6]$ features long-range order of the co-operative Jahn-Teller (JT) distortion²⁸ whereas $Cu_3[Co(CN)_6]_2$ is orbitally *disordered*,²⁹ our study provides a first insight into the effects of both vacancies and Jahn-Teller distortions on the compression mechanisms of Prussian blue analogues. Pressure is known to influence the JT distortion^{30–32} and Cu-containing Prussian blue analogues frequently show anomalous behaviour on account of the unusual bonding nature,²⁹ rendering these samples particularly interesting from a fundamental viewpoint. We use both experiment and calculation to explore the mechanical properties of PBAs, which is a relatively underexplored field, in contrast to the research devoted to understanding thermal expansion.^{28,33} To the best of our knowledge, no experimental values for the bulk moduli for any hexacyanoplatinate or hexacyanocobaltate PBA have been previously measured.

The article commences by presenting the results from the X-ray diffraction study of $Mn_3[Co(CN)_6]_2$ and $Cu_3[Co(CN)_6]_2$. $Mn_3[Co(CN)_6]_2$ transforms into a rhombohedral phase upon compression, driven by static tilts. This behaviour is not observed for the isostructural Cu analogue, which remains cubic in the pressure range studied. Next, the cubic–rhombohedral phase transition in $Mn[Pt(CN)_6]$ is discussed. This mirrors the pressure response of $Mn_3[Co(CN)_6]_2$, although it is accompanied by a much larger reduction in volume. A series of phase transitions also occurs for $Cu[Pt(CN)_6]$, but a full structural solution is beyond the scope of this study. We then show the results of density functional theory calculations, which are in good agreement with the experimental values for the compressibility and bulk modu-

lus for $Cu[Pt(CN)_6]$. To conclude, the observations are discussed in terms of the effect of vacancies, Jahn-Teller distortions, and hydration. The tilting distortions have implications for the development of new polar systems based on PBAs.

2 Experimental methods

2.1 Synthesis

An aqueous solution of the appropriate metal sulfate (typically 0.4–0.5 mmol, 0.5 ml) was added dropwise to a stoichiometric solution of $K_3Co(CN)_6$ or $K_2Pt(CN)_6$ in 0.5 ml of H_2O . In the case of $Cu[Pt(CN)_6]$ and $Cu_3[Co(CN)_6]_2$, a fine powder precipitated instantly and the reaction was stirred at 60 °C for 2 h, followed by 2 h of further stirring at ambient temperature. $Mn[Pt(CN)_6]$ formed more slowly and, hence, was subjected to 4 h stirring at 60 °C, followed by 18 h at room temperature. In all cases, the product was isolated as a fine powder—white for $Mn[Pt(CN)_6]$, pale blue-green for $Cu[Pt(CN)_6]$ and bright turquoise for $Cu_3[Co(CN)_6]_2$ —by filtration *in vacuo*. Yields were in the range 38–58%.

Single crystals of $Mn_3[Co(CN)_6]_2$ were grown by means of an H-shaped tube. Small volumes (~0.5 ml) of aqueous solutions of $K_3[Co(CN)_6]$ (43.0 mg, 0.129 mmol) and $MnSO_4 \cdot H_2O$ (21.9 mg, 0.129 mmol) were placed at each arm of the tube. Cold water was carefully added to alternate arms until the joining bridge had been filled. The tube was sealed at both ends and left undisturbed until crystals had formed.

2.2 Variable-pressure X-ray diffraction

High-pressure X-ray diffraction data were measured for the powder samples $Mn[Pt(CN)_6]$, $Cu[Pt(CN)_6]$, and $Co_3[Co(CN)_6]_2$, and for single crystals of $Mn_3[Co(CN)_6]_2$ at the ID15B beam-line of the European Synchrotron Radiation Facility, Grenoble up to 3 GPa using monochromatic X-ray radiation ($\lambda = 0.41137 \text{ \AA}$). Membrane driven LeToullec type diamond anvil cells (DACs) were used, equipped with Boehler-Almax anvils. Stainless steel was used as the gasket material, and Daphne 7373 oil was loaded as the pressure-transmitting medium. Diffraction patterns were collected with a Mar555 flat panel detector. For the single-crystal data collection, steps of 0.5° oscillation were used over a total ω -scan range of 76° about the vertical axis. Lattice parameter determination and integration of the reflection intensities were performed using the *CrysAlisPro* software.³⁴ **In the powder diffraction experiment, initial measurements revealed considerable radiation damage of the samples evident by loss of intensity and a broadening of peaks, as well as a visual black spot on the sample. This was overcome by increasing the beam size and for each pressure point, diffraction was measured both in the middle of the sample and on a pristine part in order to ensure that no significant radiation damage occurred in the centre of the sample.**

In the single-crystal loading, four different crystals were loaded, because progressive radiation damage could inhibit a possible phase transition. Thus, one crystal was measured with a full data collection involving the 0.5° step scans, while a second crystal was measured at each pressure point with a single image using a $\pm 20^\circ$ rotation in 2 s to give a single snapshot of

the diffraction spots. Initially, the effect of pressure on the diffuse scattering of $\text{Mn}_3[\text{Co}(\text{CN})_6]_2$ was followed, allowing only lattice parameter data and reciprocal space reconstructions to be determined for the ambient phase. Upon the phase transition, the beam intensity was decreased in order to perform structure solution and refinement. The single crystal structures were refined using *shelxL*, and structure solution was performed with *shelxT*, within *shelXle*.^{35–37} For the powder diffraction data, the *Dioplas* software was used to integrate the 2D area images, and *Topas academic* version 4.1 was used for Rietveld refinement.^{38,39} The pressures were measured using the ruby fluorescence method before and after each diffraction measurement. The average of both pressure values were used, in addition to the ± 0.1 GPa error to account for the error in the ruby fluorescence method in the pressure range below 10 GPa.⁴⁰

Our variable-pressure unit cell volume data for each phase were fitted with a Birch-Murnaghan equation of state (EoS) as implemented in *EoSFit7-GUI*.⁴¹ Inspection of the normalised pressure vs. Eulerian strain (f - F) plots for all phases indicate a second-order fit is sufficient to account for the experimental $p(V)$ data for all phases; where deviation from the expected behaviour (*i.e.* the pressure derivative of the bulk modulus $B' \equiv 4$) is observed visually, these fits are not well constrained and result in large uncertainties in the value of B' and B_0 . Fits to $p(V)$ data and F - f plots are given in the ESI.[‡]

2.3 Density functional theory

In order to compare with experimental data, density functional theory (DFT) calculations were used to study the structure of $\text{Cu}[\text{Pt}(\text{CN})_6]$ as a function of hydrostatic pressure. Structural relaxation was performed under pressures ranging from 0 to 2 GPa in 0.1 GPa increments. These calculations were performed within the *Abinit* software package (*v.* 8.0.8),^{42,43} using pseudopotentials and a plane-wave basis set. The Perdew–Burke–Ernzerhof exchange–correlation functional⁴⁴ was used with the *vdw*-DFT-D2 dispersion correction.⁴⁵ Optimized norm-conserving Vanderbilt pseudopotentials⁴⁶ were used as received from the *Abinit* library.⁴⁷ A 45 Ha plane-wave basis set energy cut-off and a $6 \times 6 \times 6$ Monkhorst–Pack grid⁴⁸ of *k*-points were selected by convergence studies. A metallic electron occupation scheme was employed with Methfessel–Paxton smearing.⁴⁹ Example input files are available as part of the ESI.

3 Results

3.1 $\text{M}_3[\text{Co}(\text{CN})_6]_2$, ($\text{M} = \text{Mn}^{2+}$, Cu^{2+})

$\text{Mn}_3[\text{Co}(\text{CN})_6]_2$ crystallises as a defective double perovskite, with 33% of the $\text{Co}(\text{CN})_6$ octahedra absent relative to stoichiometric systems. The ambient structure was indexed and solved in $Fm\bar{3}m$ ($a = 10.4197(3)$ Å) with weak diffuse scattering between the Bragg peaks. Fourier difference maps in the pore space indicated the presence of water, which was refined to 0.38–0.46(6) occupancy per pore, based upon different integrations. This equates to 1.8–2.1(3) H_2O per formula unit, which we note is only the pore water molecules and does not account for the water molecules that are in the $\text{Co}(\text{CN})_6$ vacancies. Single-crystal XRD data were

collected as a function of pressure up to 2.1 GPa. A transition was observed to a phase of lower symmetry due to the splitting of the diffraction reflections at $\sim 1.46(13)$ GPa (the error indicating the pressure step before and after the transition). The crystal which had previously been measured using full data collections up to 1.33 GPa did not display the transition due to the increased amount of radiation damage received. The high-pressure phase, $\text{Mn}_3[\text{Co}(\text{CN})_6]_2\text{-II}$, could be solved in $R\bar{3}$, $R\bar{3}c$ and $I2/a$. Out of these space groups, only $R\bar{3}$ leads to crystal structures with two independent metal sites, as expected for a bimetallic system, and was therefore chosen. The unit cell axes of the rhombohedral phase are related to those of the cubic aristotype by

$$\begin{bmatrix} \mathbf{a}_h \\ \mathbf{b}_h \\ \mathbf{c}_h \end{bmatrix} = \begin{bmatrix} 0.5 & 0 & -0.5 \\ -0.5 & 0.5 & 0 \\ 1 & 1 & 1 \end{bmatrix} \times \begin{bmatrix} \mathbf{a}_c \\ \mathbf{b}_c \\ \mathbf{c}_c \end{bmatrix},$$

where $(\mathbf{a}_h, \mathbf{b}_h, \mathbf{c}_h)$ and $(\mathbf{a}_c, \mathbf{b}_c, \mathbf{c}_c)$ denote the lattice vectors for the trigonal space group (in the hexagonal setting) and the cubic space group, respectively. $R\bar{3}$ symmetry is consistent with an $a^-a^-a^-$ (irrep Γ_4^+) tilt system in Glazer notation [Fig. 2(a)].^{14,50} In contrast to other molecular perovskites, octahedral tilting is relatively uncommon in PBAs.^{27,51,52} Similar diffuse scattering to the ambient phase was observed in the high-pressure phase.

To facilitate easy comparison between the structures of the two phases, the framework can be parametrised by the strut length, r (*i.e.* the Co–CN–Mn–CN–Co length), and the hingeing angle, θ , as developed in Ref. 53. In the cubic phase, the strut length is equivalent to the lattice parameter and the angle is 90° by symmetry. In the rhombohedral phase, we have

$$r = \frac{1}{3}(2\sqrt{3}a_h + c_h) \quad (1)$$

and

$$\theta = \cos^{-1} \left(\frac{r^2 - 2a_h^2}{r^2} \right), \quad (2)$$

where a_h and c_h are the lattice parameters of the trigonal phase in the hexagonal setting. A plot of the percentage changes in r , θ and the reduced volume (V/Z) as a function of the pressure is given in Fig. 3. The strut length decreases monotonically upon compression, likely due to a combination of bond compression and dynamic tilting. There is no significant discontinuity in the strut length at the transition point, whereas there is a small step change in the hingeing angle. The compressibility (K) of r can be calculated by

$$K = -\frac{1}{r} \frac{dr}{dp}, \quad (3)$$

where p is the pressure. This yields values of $21.4(9)$ TPa^{-1} and $16.4(7)$ TPa^{-1} for the ambient and high-pressure phase, respectively. Due to the low number of points for the high-pressure phase, data collected both on compression and decompression were used for the fitting (see ESI), although only data from the compression are plotted here. These values for the compressibilities are in the same range as those observed for related molecular perovskites based on the formate ligand.^{54,55} The lattice parameters were fit by a 2nd order Birch–Murnaghan plot^{56,57} to give

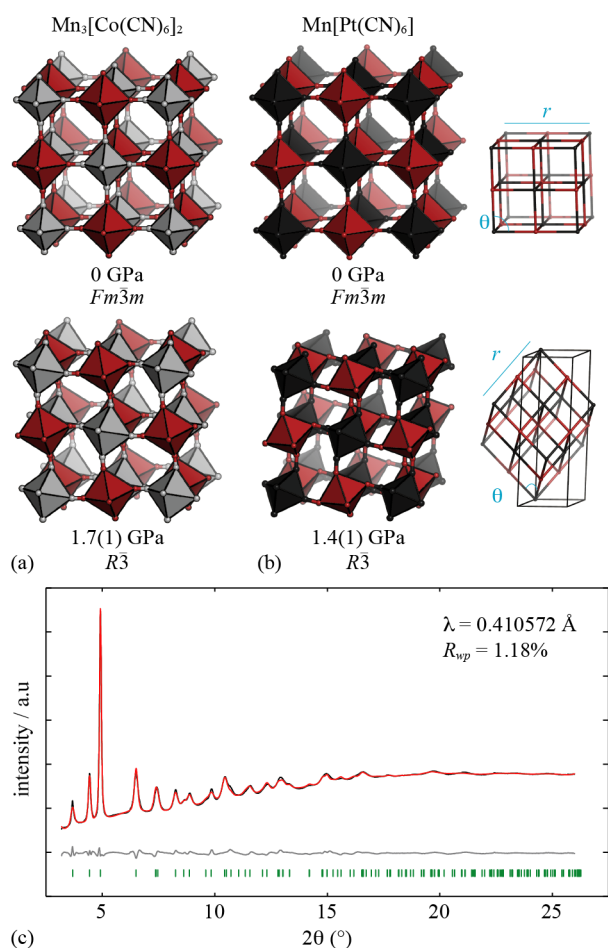


Fig. 2 The ambient and high-pressure structures of (a) $\text{Mn}_3[\text{Co}(\text{CN})_6]_2$ and (b) $\text{Mn}[\text{Pt}(\text{CN})_6]$. The strut lengths and hinge angle relative to the unit cells of the two phases are also shown. (c) Powder X-ray diffraction pattern for $\text{Mn}[\text{Pt}(\text{CN})_6]$ measured at 1.43 GPa (black line) and Rietveld fit (red line), with difference (data – fit) shown in grey. The allowed reflections in $R\bar{3}$ are shown in green.

$B_0 = 13.5(6)$ GPa and $B_0 = 14(2)$ GPa for the two phases. These values are lower than what has been reported for other PBAs^{22,26} and imply that $\text{Mn}_3[\text{Co}(\text{CN})_6]_2$ is soft in comparison.

$\text{Cu}_3[\text{Co}(\text{CN})_6]_2$ is isostructural to its Mn counterpart and shows no long-range order of the Jahn-Teller distortions. Single crystals were not accessible for this compound nor for any of the compounds discussed below and so the measurements were carried out on polycrystalline samples. As PBAs are prone to radiation damage, two data collections per pressure point were performed: one in the centre of the sample and one on a pristine part without previous X-ray exposure, in order to discern any pressure- and radiation-induced effects. The lattice parameters did not vary significantly between the two measurements and here, the data from the collections at the central part of the DAC are used. In contrast to $\text{Mn}_3[\text{Co}(\text{CN})_6]_2$, $\text{Cu}_3[\text{Co}(\text{CN})_6]_2$ remains cubic throughout the entire pressure range studied without any phase transitions [Fig. 3]. The strut compressibility and bulk modulus are calculated as $8.19(14)$ TPa^{-1} and $35.0(5)$ GPa and hence this system is noticeably stiffer than the Mn analogue. These values can

be compared to the bulk moduli of $43(2)$ GPa reported for a hexacyanoferrate in Ref. 26.

3.2 $\text{M}[\text{Pt}(\text{CN})_6]$, ($\text{M} = \text{Mn}^{2+}, \text{Cu}^{2+}$)

$\text{Mn}[\text{Pt}(\text{CN})_6]$ crystallises as an A-site deficient double perovskite (ReO_3 topology) with space group $Fm\bar{3}m$ in the low-pressure regime. It compresses monotonically until a phase transition at $1.31(10)$ GPa (the error indicating the pressure step before and after the transition). The percentage change in r is lower than for $\text{Mn}_3[\text{Co}(\text{CN})_6]_2$, which may be a result of the lack of vacancies. The new phase, $\text{Mn}[\text{Pt}(\text{CN})_6]\text{-II}$, could be indexed in $R\bar{3}$ and a structural model was found through Rietveld refinement, with the rhombohedral phase of $\text{Mn}_3[\text{Co}(\text{CN})_6]_2$ as a starting model [Fig. 2(b)–(c)]. $R\bar{3}m$ features the same systematic absences as $R\bar{3}$ and so fits the data equally well, but gives a nonsensical structure. $\text{Mn}[\text{Pt}(\text{CN})_6]\text{-II}$ is considerably more distorted than $\text{Mn}_3[\text{Co}(\text{CN})_6]_2\text{-II}$, with tilt angles (*i.e.* the Pt–Mn–N angle, which is 0° in the absence of static octahedral tilts) of $\sim 23^\circ$. In contrast, the angle in $\text{Mn}_3[\text{Co}(\text{CN})_6]_2\text{-II}$ amounts to $\sim 13^\circ$. The large amplitude of the tilting distortion in combination with significant discontinuous changes in r and θ lead to a larger volume reduction upon the transition than in the hexacyanocobaltate [Fig. 3]. Moreover, the rhombohedral $\text{Mn}[\text{Pt}(\text{CN})_6]\text{-II}$ is softer than the cubic $\text{Mn}[\text{Pt}(\text{CN})_6]\text{-I}$, with the compressibility of r nearly doubling in magnitude: from $8.92(19)$ TPa^{-1} to $18(1)$ TPa^{-1} and the bulk moduli softening from $35(2)$ to $9.31(1.4)$ GPa. This increased softening occurs due to the tilting of the octahedra, allowing much greater reduction in volume compared to the bond compression mechanism observed in the ambient phase. Similar “flexibility transitions” also occur in the framework $\text{Cu}(\text{tcm})$ ($\text{tcm} = \text{tricyanomethanide}$, $\text{C}(\text{CN})_3^-$) as well as in some ceramic perovskites.^{58,59} The behaviour contrasts with the results of Ref. 22, where the high-pressure phases of a series of PBAs ($\text{Rb}_{0.85}\text{Zn}[\text{Fe}(\text{CN})_6]_{0.95} \cdot 1.5\text{H}_2\text{O}$ and $\text{Rb}_{0.64}\text{Zn}[\text{Fe}(\text{CN})_6]_{0.88} \cdot 3.5\text{H}_2\text{O}$) were found to be stiffer than the ambient phases. However, in these reported transitions, the cubic symmetry is not reduced, and a discontinuity is only visible in the Raman spectra, indicating only a change in the vibrational behaviour of the CN ligands.

$\text{Cu}[\text{Pt}(\text{CN})_6]$ is a rare example of a non-cubic PBA, as a result of the cooperative Jahn-Teller distortion that lowers the symmetry to the maximal subgroup $I4/mmm$ with unit cell dimensions related to the aristotype cell (a_0) by $a = b \sim \frac{1}{\sqrt{2}}a_0$ and $c \sim a_0$. The c -axis comprises the long JT-distorted bonds while the normalised a -axis consists of the short bonds from the $\text{Cu}(\text{CN})_6$ octahedra. The deviation from cubic symmetry is therefore a direct measure of the magnitude of the Jahn-Teller distortion. $\text{Cu}[\text{Pt}(\text{CN})_6]$ compresses anisotropically with the c -axis being ~ 3 times softer than the a -axis ($K_c = 15.3(3)$ TPa^{-1} and $K_a = 4.82(11)$ TPa^{-1}). As a result, the Jahn-Teller distortion becomes less pronounced upon increasing pressure—a phenomenon also observed in other Jahn-Teller distorted systems.^{31,54,60} The bulk modulus is $37(3)$ GPa, consistent with the values for the other compounds reported here. A phase transition occurred at $1.09(15)$ GPa, accompanied by broadening and a significant overlap of the reflections. Attempts to solve the

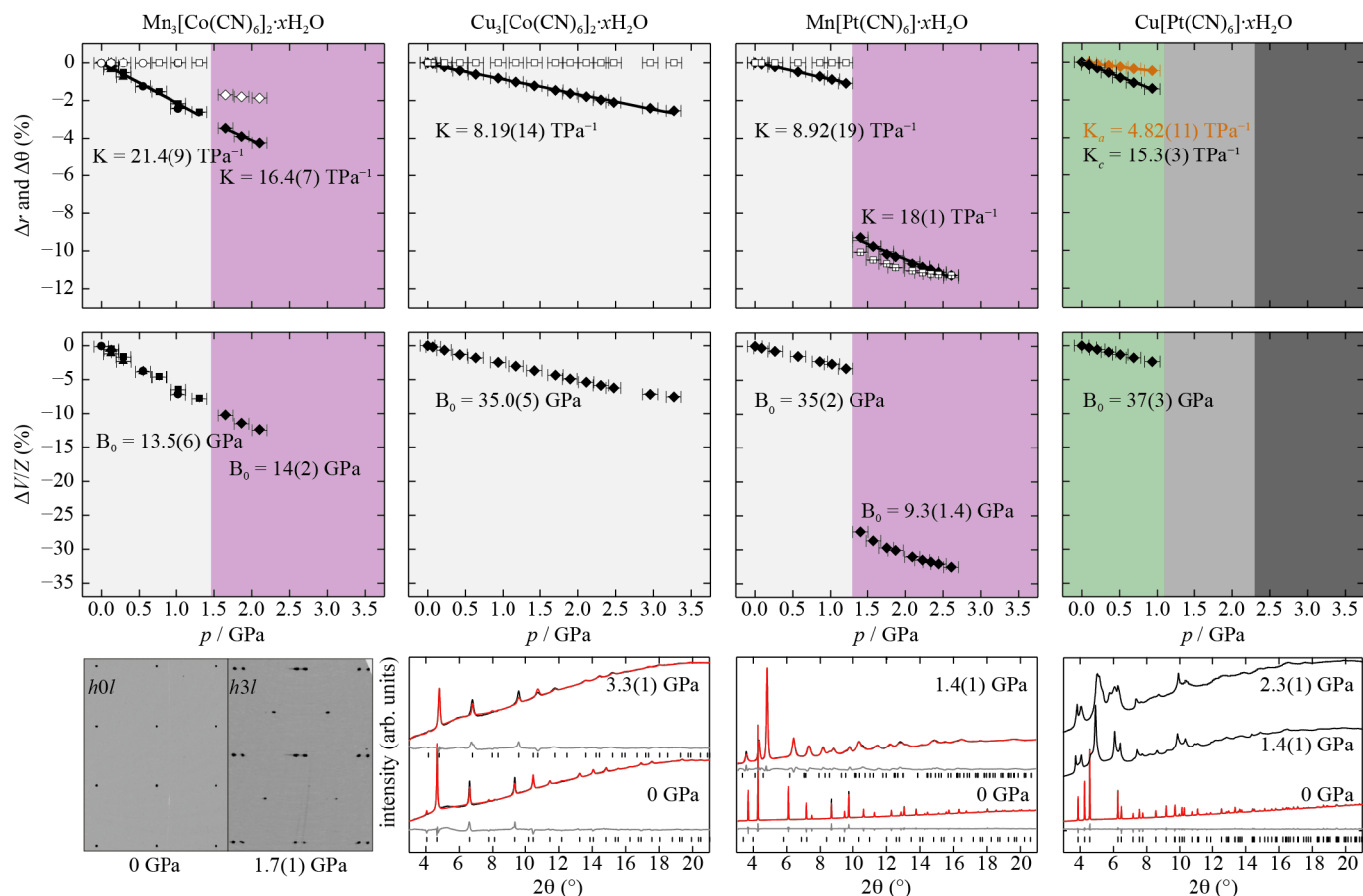


Fig. 3 The percentage changes in the strut length r (filled symbols), hingeing angle θ (open symbols), and the reduced volume V/Z along with the fits used to calculate the compressibilities and bulk moduli. For $\text{Cu}[\text{Pt}(\text{CN})_6]$, the strut length along a (yellow) and c (black) are shown. For $\text{Mn}_3[\text{Co}(\text{CN})_6]_2$, the different symbols correspond to different crystals and only the data collected upon compression are plotted. The background colours indicate the crystal system of the phases, with cubic shown in light grey, rhombohedral in purple and tetragonal in green. The dark grey colours of $\text{Cu}[\text{Pt}(\text{CN})_6]$ correspond to unsolved low-symmetry phases. Rietveld fits of the diffraction patterns at different pressures are also shown.

structure proved unsuccessful. The crystallites without previous X-ray exposure underwent a second phase transition at higher pressure (see ESI), suggesting that this phase transition is inhibited by radiation damage. All transitions were reversible upon release of pressure.

DFT calculations at finite strain for $\text{Cu}[\text{Pt}(\text{CN})_6]$ gave a bulk modulus of 37.0(2) GPa, $K_a = 3.5 \text{ TPa}^{-1}$ and $K_c = 17.8 \text{ TPa}^{-1}$, all of which are in good agreement with experimental values. Similar calculations were considerably more challenging for the other systems, presumably due to the larger number of unpaired electrons and presence of defects and disorder. The elastic tensor of $\text{Cu}[\text{Pt}(\text{CN})_6]$ was also calculated directly using density functional perturbation theory⁶¹ to give

$$\begin{pmatrix} 97.9 & 86.1 & 20.0 & & & \\ 86.1 & 97.9 & 20.0 & & & \\ 20.0 & 20.0 & 48.4 & & & \\ & & & 4.68 & & \\ & & & & 4.68 & \\ & & & & & 44.2 \end{pmatrix}. \quad (4)$$

The elastic tensor corresponds to a bulk modulus of 40.3 GPa, which is consistent with the experimental result (35(2) GPa) and

with that from the calculations performed using finite strains mentioned above. The Voigt-Reuss-Hill averaged⁶² values for the effective polycrystalline Young's modulus, shear modulus, and Poisson ratio are 50.1 GPa, 18.6 GPa, and 0.34, respectively.

The anisotropy of the Young's modulus and Poisson ratio is shown in Fig. 4. $\text{Cu}[\text{Pt}(\text{CN})_6]$ displays a considerable elastic anisotropy, with a universal anisotropy index of 7.7.⁶³ The anisotropy of the Young's modulus is closely related to the structure, with the stiffest directions coinciding with the cyanide linkages along [110]. The Jahn-Teller distortion leads to a significant softening of the [001] direction by comparison to [110]. The mismatch of unit cell axes and the directions of maximum stiffness has been associated with anomalous mixed negative and positive thermal expansion⁶⁴ as seen in $\text{Cu}[\text{Pt}(\text{CN})_6]$.²⁸ The anisotropic Poisson ratios indicate strong elastic coupling between the a and b -axes and weak coupling between c and other directions, again demonstrating the strong effect of the Jahn-Teller distortion on the elastic properties.

4 Discussion and conclusions

This study has investigated the pressure response of a series of Prussian blue analogues with and without structural defects and

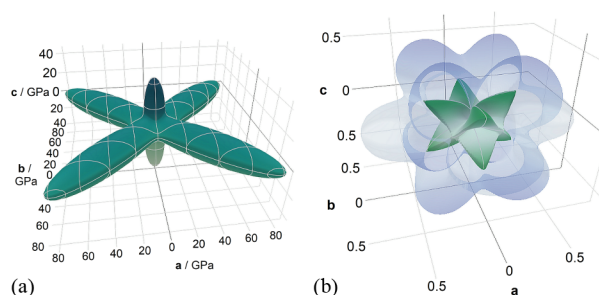


Fig. 4 Anisotropic Young's modulus (left) and Poisson ratio (right) in $\text{Cu}[\text{Pt}(\text{CN})_6]$. The Young's modulus in a given direction is shown as a cyan surface; the maximum Poisson ratio in a given direction is shown as a transparent blue surface while the minimum is shown as a green surface. Visualisation generated using ELATE.⁶⁵

Jahn-Teller distortions, attempting to elucidate the role played by each degree of freedom in the compression behaviour. The systems remain in their ambient phases until ~ 1.1 – 1.4 GPa where phase transitions occur for all but the orbitally active and defective $\text{Cu}_3[\text{Co}(\text{CN})_6]_2$. This particular compound exhibits orbital disorder which perhaps plays a role in inhibiting the onset of a phase transition. The long axes of a Jahn-Teller distorted octahedron are appreciably softer than the horizontal plane comprising the short bonds. As the disordered structure features orientational disorder of these soft long axes, a significant volume reduction can occur without the need for a phase transition. However, this argument is speculative and the lack of a phase transition may also be the result of a different hydration state of $\text{Cu}_3[\text{Co}(\text{CN})_6]_2$, the exact level of which is unknown, relative to the other compounds.²⁹

The cubic–rhombohedral phase transitions displayed by the Mn-containing systems verifies the presence of pressure-induced octahedral tilts in PBAs, as indicated by several spectroscopic studies.^{21–23,26} The magnitude of the tilts is—perhaps surprisingly—smaller in the defective $\text{Mn}_3[\text{Co}(\text{CN})_6]_2$ relative to the fully connected $\text{Mn}[\text{Pt}(\text{CN})_6]$. **As a result, $\text{Mn}[\text{Pt}(\text{CN})_6]$ exhibits a large volume reduction across the phase transition that is not mirrored by the corresponding cobaltate.** Whether these differences are due to intrinsic different degrees of flexibility of the frameworks or external factors, such as hydration levels, is not yet clear. **We note that the amplitude of the vibrational modes in the related hexacyanoplatinate $\text{Cd}[\text{Pt}(\text{CN})_6]$ is dampened by the presence of interstitial solvent species through increased steric repulsion.⁶⁶ It should also be considered whether the vacancies may disrupt the percolation of correlated tilts to some extent.**

The extent of compression in r prior to the phase transitions occur can be **speculatively** related to the presence of vacancies. **The defect-free hexacyanoplatinates compress less ($\sim 1\%$ in r) than the defective $\text{Mn}_3[\text{Co}(\text{CN})_6]_2$ ($\sim 2.5\%$) before the onset of a phase transition [Fig. 3]. Vacancies increase the free space of the framework and so presumably facilitate the contraction of the strut lengths. As a result, the defective frameworks should be able to sustain a larger strut compression on average than the non-defective systems, as observed. When the compression of r reaches a threshold value, the symmetry-breaking tilting emerges**

to maintain the volume reduction. The defective $\text{Cu}_3[\text{Co}(\text{CN})_6]_2$ remained in the ambient phase up to ~ 3 GPa, yet the reduction in r at the highest pressure point is comparable to that of $\text{Mn}_3[\text{Co}(\text{CN})_6]_2$ prior to the transition. This implies that a phase transition may indeed occur for $\text{Cu}_3[\text{Co}(\text{CN})_6]_2$ above 3 GPa; however, the solidification of the pressure-transmitting medium limited the available pressure range. Variable-pressure studies with different media so as to allow for the exploration higher pressures would be of interest.

There is an emerging interest in molecular perovskites with ferroelectric properties^{67–70} and, in light of this, the tilt patterns discovered here are of particular interest. In so-called hybrid improper ferroelectricity, two or more structural distortions are coupled such that the global inversion symmetry is broken and a polar mode appears.⁷¹ PBAs with A-site cation order commonly crystallise in $F\bar{4}3m$,^{33,72} and the additional symmetry lowering induced by the $a^-a^-a^-$ tilting—as we observe here—leads to the polar, and potentially ferroelectric, space group $R3$. By consequence, such systems can be expected to exhibit ferroelectric properties under the application of modest pressures. Furthermore, if these pressure-induced tilts are accessible in PBAs with organic A-site cations (cyanoelapsolites), a larger range of polar couplings are attainable. For example, an R-point arrangement of a quadrupolar cation will achieve a similar effect as the cation order in $F\bar{4}3m$.⁷⁰ All A-site cations with prolate or oblate symmetry (*i.e.* rod-like or disc-like cations) possess a quadrupolar moment and this includes very common species such as methylammonium or imidazolium, which have successfully been incorporated on the A-site of an organic PBA.^{73,74} Hence, the activation of rigid unit modes by means of pressure may have consequences for the search for new ferroelectric materials.

The powder samples $\text{Cu}_3[\text{Co}(\text{CN})_6]_2$, $\text{Mn}[\text{Pt}(\text{CN})_6]$, and $\text{Cu}[\text{Pt}(\text{CN})_6]$ exhibit similar bulk moduli within error, whereas the single crystal of $\text{Mn}_3[\text{Co}(\text{CN})_6]_2$ is considerably softer. The invariance of the bulk moduli to composition for the polycrystalline samples can be contrasted with the results from literature, where moduli from 17 to 71 GPa have been reported for PBAs of varying composition.^{22,27} However, it is not clear to what extent this large range of values reflects a genuine compositional dependence of the compressibility behaviour as opposed to a sensitivity to different fitting methods and considerations such as synthesis conditions and water content. All samples in this study were measured as-synthesised and therefore contain a certain amount of solvent (H_2O) from the synthesis. Moreover, to note that the polycrystalline powders were stored in air within glass vials, while the single crystals were in oil. The inclusion of guest solvent into the pores of MOFs and zeolites during hydrostatic compression—a process referred to as hypersaturation—has a significant effect on the pressure response^{75–78} and a related effect can be anticipated for Prussian blue analogues. The hydration level likely depends on the synthesis conditions and so presumably differs between powders and single crystals, which may explain the dissimilar bulk moduli. Yet, it is clear that the behaviour of PBAs is governed by an intimate interplay between the vacancies, hydration, compositions and Jahn-Teller distortions. Future studies on dehydrated samples will be of value, in order to unravel the

precise role played by each of these degrees of freedom.

Conflict of interest

There are no conflicts to declare.

Acknowledgements

This research was carried out at the European Synchrotron Radiation Facility on the beamline ID15B. Computational resources were provided by the University of Oxford, Department of Chemistry, and the UK's HEC Materials Chemistry Consortium, which is funded by the EPSRC (EP/L000202). This work used the ARCHER UK National Supercomputing Service (<http://www.archer.ac.uk>).

References

- 1 D. S. Middlemiss, D. Portinari, C. P. Grey, C. A. Morrison and C. C. Wilson, *Phys. Rev. B*, 2010, **81**, 184410.
- 2 M. Kabir and K. J. Van Vliet, *Phys. Rev. B*, 2012, **85**, 054431.
- 3 J. M. Herrera, A. Bachschmidt, F. Villain, A. Bleuzen, V. Marvaud, W. Wernsdorfer and M. Verdaguer, *Phil. Trans. R. Soc. A.*, 2008, **366**, 127–138.
- 4 J. Jiménez-Gallegos, J. Rodríguez-Hernández, H. Yee-Madeira and E. Reguera, *J. Phys. Chem. C*, 2010, **114**, 5043–5048.
- 5 J. Balmaseda, E. Reguera, J. Rodríguez-Hernández, L. Reguera and M. Autie, *Micropor. Mesopor. Mater.*, 2006, **96**, 222–236.
- 6 L. Shen, Z. Wang and L. Chen, *Chem. Eur. J.*, 2014, **20**, 12559–12562.
- 7 P. Padigi, J. Thiebes, M. Swan, G. Goncher, D. Evans and R. Solanki, *Electrochim. Acta*, 2015, **166**, 32–39.
- 8 H. J. Buser, D. Schwarzenbach, W. Petter and A. Ludi, *Inorg. Chem.*, 1977, **16**, 2704–2710.
- 9 H. Tokoro and S.-i. Ohkoshi, *Dalton Trans.*, 2011, **40**, 6825–6833.
- 10 H.-J. Buser, G. Ron and A. Ludi, *J. Chem. Soc. Faraday Trans.*, 1974, 2473–2474.
- 11 M. Verdaguer, A. Bleuzen, V. Marvaud, J. Vaissermann, M. Seuleiman, C. Desplanches, A. Scullier, C. Train, R. Garde, G. Gelly, C. Lomenech, I. Rosenman, P. Veillet, C. Cartier and F. Villain, *Coord. Chem. Rev.*, 1999, **190–192**, 1023–1047.
- 12 H. Zhang, C. Li, D. Chen, J. Zhao, X. Jiao and Y. Xia, *CrystEngComm*, 2017, **19**, 2057–2064.
- 13 S. S. Kaye and J. R. Long, *J. Am. Chem. Soc.*, 2005, **127**, 6506–6507.
- 14 A. M. Glazer, *Acta Crystallogr. B Struct. Cryst. Cryst. Chem.*, 1972, **28**, 3384–3392.
- 15 C. J. Howard and H. T. Stokes, *Acta Crystallogr. B Struct. Sci.*, 1998, **54**, 782–789.
- 16 S. G. Duyker, J. A. Hill, C. J. Howard and A. L. Goodwin, *J. Am. Chem. Soc.*, 2016, **138**, 11121–11123.
- 17 M. T. Dove, V. Heine and K. D. Hammonds, *Mineral. Mag.*, 1995, **59**, 629–639.
- 18 J. Z. Tao and A. W. Sleight, *J. Solid State Chem.*, 2003, **173**, 442–448.
- 19 G. Kieslich and A. L. Goodwin, *Mater. Horiz.*, 2017, **4**, 362–366.
- 20 H. L. B. Boström, J. A. Hill and A. L. Goodwin, *Phys. Chem. Chem. Phys.*, 2016, **18**, 31881–31894.
- 21 X. Liu, Y. Moritomo, T. Matsuda, H. Kamioka, H. Tokoro and S.-i. Ohkoshi, *J. Phys. Soc. Jpn.*, 2009, **78**, 013602.
- 22 T. Matsuda, X. Liu, T. Shibata, H. Kamioka, Y. Ohishi and Y. Moritomo, *J. Phys. Soc. Jpn.*, 2009, **78**, 105002.
- 23 J.-D. Cafun, J. Lejeune, J.-P. Itié, F. Baudalet and A. Bleuzen, *J. Phys. Chem. C*, 2013, **117**, 19645–19655.
- 24 M. Sugimoto, S. Yamashita, H. Akutsu, Y. Nakazawa, J. G. DaSilva, C. M. Kareis and J. S. Miller, *Inorg. Chem.*, 2017, **56**, 10452–10457.
- 25 M. Ohba, W. Kaneko, S. Kitagawa, T. Maeda and M. Mito, *J. Am. Chem. Soc.*, 2008, **130**, 4475–4484.
- 26 A. Bleuzen, J.-D. Cafun, A. Bachschmidt, M. Verdaguer, P. Münsch, F. Baudalet and J.-P. Itié, *J. Phys. Chem. C*, 2008, **112**, 17709–17715.
- 27 Y. Moritomo, M. Hanawa, Y. Ohishi, K. Kato, M. Takata, A. Kuriki, E. Nishibori, M. Sakata, S. Ohkoshi, H. Tokoro and K. Hashimoto, *Phys. Rev. B*, 2003, **68**, 144106.
- 28 K. W. Chapman, P. J. Chupas and C. J. Kepert, *J. Am. Chem. Soc.*, 2006, **128**, 7009–7014.
- 29 E. Reguera, J. Rodríguez-Hernández, A. Champi, J. G. Duque, E. Granado and C. Rettori, *Z. Phys. Chem.*, 2006, **220**, 1609–1619.
- 30 G. J. Halder, K. W. Chapman, J. A. Schlueter and J. L. Manson, *Angew. Chem. Int. Ed.*, 2011, **50**, 419–421.
- 31 K. Caslin, R. K. Kremer, F. S. Razavi, M. Hanfland, K. Syassen, E. E. Gordon and M.-H. Whangbo, *Phys. Rev. B*, 2016, **93**, 022301.
- 32 M. W. Lufaso, W. R. Gemmill, S. J. Mugavero III, Y. Lee, T. Vogt and H.-C. zur Loye, *J. Solid State Chem.*, 2006, **179**, 3556–3561.
- 33 S. Adak, L. L. Daemen, M. Hartl, D. Williams, J. Summerhill and H. Nakotte, *J. Solid State Chem.*, 2011, **184**, 2854–2861.
- 34 *Rigaku Oxford Diffraction*, (2018), *CrysAlisPro Software system, version 1.171.38.46*, Rigaku Corporation, Oxford, UK.
- 35 G. M. Sheldrick, *Acta Cryst. C*, 2015, **71**, 3–8.
- 36 G. M. Sheldrick, *Acta Cryst. A*, 2015, **71**, 3–8.
- 37 C. B. Hübschle, G. M. Sheldrick and B. Dittrich, *J. Appl. Crystallogr.*, 2011, **44**, 1281–1284.
- 38 C. Prescher and V. B. Prakapenka, *High Pressure Res.*, 2015, **35**, 223–230.
- 39 A. A. Coelho, *TOPAS-Academic, version 4.1 (computer software)*, Coelho Software, Brisbane.
- 40 J. M. Recio, J. M. Menéndez and A. O. de la Roza, *An Introduction to High-Pressure Science and Technology*, CRC Press, 2016.
- 41 R. J. Angel, M. Alvaro and J. Gonzalez-Platas, *Z. Kristallogr.*, 2014, **229**, 405–419.
- 42 X. Gonze, F. Jollet, F. Abreu Araujo, D. Adams, B. Amadon, T. Applencourt, C. Audouze, J.-M. Beuken, J. Bieder, A. Bokhanchuk, E. Bousquet, F. Bruneval, D. Caliste, M. Côté,

- F. Dahm, F. Da Pieve, M. Delaveau, M. Di Gennaro, B. Dorado, C. Espejo, G. Geneste, L. Genovese, A. Gerossier, M. Giantomassi, Y. Gillet, D. R. Hamann, L. He, G. Jomard, J. Laflamme Janssen, S. Le Roux, A. Levitt, A. Lherbier, F. Liu, I. Lukačević, A. Martin, C. Martins, M. J. T. Oliveira, S. Poncé, Y. Pouillon, T. Rangel, G.-M. Rignanese, A. H. Romero, B. Rousseau, O. Rubel, A. A. Shukri, M. Stankovski, M. Torrent, M. J. Van Setten, B. Van Troeye, M. J. Verstraete, D. Waroquiers, J. Wiktor, B. Xu, A. Zhou and J. Zwanziger, *Comput. Phys. Commun.*, 2016, **205**, 106–131.
- 43 F. Bottin, S. Leroux, A. Knyazev and G. Zerah, *Comput. Mater. Sci.*, 2008, **42**, 329–336.
- 44 J. P. Perdew, K. Burke and M. Ernzerhof, *Phys. Rev. Lett.*, 1996, **77**, 3865–3868.
- 45 S. Grimme, *J. Comput. Chem.*, 2006, **27**, 1787–1799.
- 46 D. R. Hamann, *Phys. Rev. B*, 2013, **88**, 085117.
- 47 www.abinit.org/psp-tables.
- 48 H. J. Monkhorst and J. D. Pack, *Phys. Rev. B*, 1976, **13**, 5188–5192.
- 49 M. Methfessel and A. T. Paxton, *Phys. Rev. B*, 1989, **40**, 3616–3621.
- 50 C. J. Howard, B. J. Kennedy and P. M. Woodward, *Acta Crystallogr. B Struct. Sci.*, 2003, **59**, 463–471.
- 51 J.-H. Her, P. W. Stephens, C. M. Kareis, J. G. Moore, K. S. Min, J.-W. Park, G. Ball, B. S. Kennon and J. S. Miller, *Inorg. Chem.*, 2010, **49**, 1524–1534.
- 52 T. Matsuda, J. Kim and Y. Moritomo, *Dalton Trans.*, 2012, **41**, 7620–7623.
- 53 J. M. Ogborn, I. E. Collings, S. A. Moggach, A. L. Thompson and A. L. Goodwin, *Chem. Sci.*, 2012, **3**, 3011–3017.
- 54 I. E. Collings, M. Bykov, E. Bykova, M. Hanfland, S. van Smaalen, L. Dubrovinsky and N. Dubrovinskaia, *CrystEngComm*, 2018, **20**, 3512–3521.
- 55 S. Sobczak, A. Chitnis, M. Andrzejewski, M. Mączka, S. Gohil, N. Garg and A. Katrusiak, *CrystEngComm*, 2018, **20**, 5348–5355.
- 56 F. Birch, *Phys. Rev.*, 1947, **71**, 809–824.
- 57 F. D. Murnaghan, *Proc. Natl. Acad. Sci. U.S.A.*, 1944, **30**, 244–247.
- 58 S. J. Hunt, M. J. Cliffe, J. A. Hill, A. B. Cairns, N. P. Funnell and A. L. Goodwin, *CrystEngComm*, 2015, **17**, 361–369.
- 59 G. Thornton, B. C. Tofield and A. W. Hewat, *J. Solid State Chem.*, 1986, **61**, 301–307.
- 60 J.-S. Zhou, J. A. Alonso, J. T. Han, M. T. Fernández-Díaz, J.-G. Cheng and J. B. Goodenough, *J. Fluorine Chem.*, 2011, **132**, 1117–1121.
- 61 D. R. Hamann, X. Wu, K. M. Rabe and D. Vanderbilt, *Phys. Rev. B*, 2005, **71**, 035117.
- 62 H. M. Ledbetter, *J. Appl. Phys.*, 1973, **44**, 1451–1454.
- 63 S. I. Ranganathan and M. Ostoja-Starzewski, *Phys. Rev. Lett.*, 2008, **101**, 055504.
- 64 C. P. Romao, *Phys. Rev. B*, 2017, **96**, 134113.
- 65 R. Gaillac, P. Pullumbi and F.-X. Coudert, *J. Phys.: Condens. Matter*, 2016, **28**, 275201.
- 66 A. L. Goodwin, K. W. Chapman and C. J. Kepert, *J. Am. Chem. Soc.*, 2005, **127**, 17980–17981.
- 67 A. Stroppa, P. Jain, P. Barone, M. Marsman, J. M. Perez-Mato, A. K. Cheetham, H. W. Kroto and S. Picozzi, *Angew. Chem. Int. Ed.*, 2011, **50**, 5847–5850.
- 68 D. Di Sante, A. Stroppa, P. Jain and S. Picozzi, *J. Am. Chem. Soc.*, 2013, **135**, 18126–18130.
- 69 G. Kieslich, S. Kumagai, A. C. Forse, S. Sun, S. Henke, M. Yamashita, C. P. Grey and A. K. Cheetham, *Chem. Sci.*, 2016, **7**, 5108–5112.
- 70 H. L. B. Boström, M. S. Senn and A. L. Goodwin, *Nat. Commun.*, 2018, **9**, 2380.
- 71 N. A. Benedek and C. J. Fennie, *Phys. Rev. Lett.*, 2011, **106**, 107204.
- 72 S.-i. Ohkoshi, H. Tokoro and K. Hashimoto, *Coord. Chem. Rev.*, 2005, **249**, 1830–1840.
- 73 M. Rok, J. K. Prytys, V. Kinzhybalo and G. Bator, *Dalton Trans.*, 2017, **46**, 2322–2331.
- 74 W. Zhang, Y. Cai, R.-G. Xiong, H. Yoshikawa and K. Awaga, *Angew. Chem. Int. Ed.*, 2010, **49**, 6608–6610.
- 75 R. M. Hazen, *Science*, 1983, **219**, 1065–1067.
- 76 R. M. Hazen and L. W. Finger, *J. Appl. Phys.*, 1984, **56**, 1838–1840.
- 77 K. W. Chapman, G. J. Halder and P. J. Chupas, *J. Am. Chem. Soc.*, 2008, **130**, 10524–10526.
- 78 A. J. Graham, J.-C. Tan, D. R. Allan and S. A. Moggach, *Chem. Commun.*, 2012, **48**, 1535–1537.